

Detection of densely dispersed spherical bubbles in digital images based on a template matching technique

Application to wet foams

X. Zabulis^{a,b,*}, M. Papara^a, A. Chatziargyriou^{a,b}, T.D. Karapantsios^a

^a Division of Chemical Technology, School of Chemistry, Aristotelian University of Thessaloniki, University Box 116, 54124 Thessaloniki, Greece

^b Informatics and Telematics Institute, Centre for Research and Technology Hellas, 1st Km Thermi-Panorama Road, 57001 Thessaloniki, Greece

Received 2 October 2006; received in revised form 23 December 2006; accepted 2 January 2007

Available online 13 January 2007

Abstract

This work describes a, single-camera, bubble measurement system, which features a template-based detection method. The motivation for the proposed approach is the poor performance of conventional methods towards bubble and particle detection in dense dispersions. The, poor, performance of such conventional approaches is reviewed, demonstrated and explained. The proposed approach utilizes templates to increase robustness and an image scale-space to detect bubbles independently of their size. Furthermore, algorithmic optimizations for the proposed approach that target the reduction of computational complexity and user-intervention are proposed and compiled into a software application. This software is then tested in the determination of bubble size distribution in decaying wet foam.

© 2007 Elsevier B.V. All rights reserved.

Keywords: Bubble size; Bubble size distribution; Foam; Image analysis; Template matching; Particle detection; Image correlation; Scale-space

1. Introduction

This work concerns non-intrusive, or passive, optical imaging methods for the spatial measurement of bubbles, droplets, or particles (henceforth, globally referred to as particles) in dense dispersions. Among them, optical methods are preferred due to their superb spatial resolution. Passive methods are frequently required when the studied phenomena are sensitive to intervention of intrusive measuring probes. Non-optical, methods are limited by the relatively coarser spatial granularity of the spatial arrays in which e.g. electromagnetic sensors are arranged. These passive methods find better application in measuring bulk particle motion [1–3]. Similarly, optical velocimetry methods (e.g. [4–9]) utilize statistical properties of small image regions (e.g. optical flow) to volumetrically estimate average velocity at each point in space.

Optical tomography methods have been reported for the analysis of 3D foams [10,11]. These methods utilize a series of images at different focal distances that are acquired simultaneously (or synchronously enough for the studied phenomenon) to obtain 3D representations of particle systems. In [12–14] modulating the focus of a still camera while acquiring images of a nearly motionless polyhedral foam structure produces a series of images in which particle silhouettes come in and out of focus, as a function of the depth field. Then, detecting the image at which a particle is focused best, provides the cue to its distance—see [15] for a review on optical tomography systems. Although tomographic methods have been successful for the analysis of quasi-stable dry foams, it is doubtful whether they could be as effective with unstable wet foams. In these cases, not only synchronous measurements are tedious but also the intense curvature of the gas/liquid interfaces and the finite size of Plateau borders can highly distort the images away from the foam boundaries. In more stable foams, tomographic methods have been combined with 360° X-ray tomography along the depth to acquire a clear image of the particle outline at each level of depth [16–18].

A central problem in both tomography-based or simple optical measurement methods is the detection of the particle, which

* Corresponding author at: Informatics and Telematics Institute, Centre for Research and Technology Hellas, 1st Km Thermi-Panorama Road, 57001 Thessaloniki, Greece. Tel.: +30 2310464160; fax: +30 2310464164.

E-mail addresses: xenophon@iti.gr (X. Zabulis), mariapa@chem.auth.gr (M. Papara), achatzia@iti.gr (A. Chatziargyriou), karapant@chem.auth.gr (T.D. Karapantsios).

is hindered by numerous factors/effects such as occlusions, highlights, image clarity, imaging distortions and artifacts, etc.—see [19] for a review of the specific problems arising in the analysis of foam images. The approach proposed in this paper, is applicable to the case of detecting particles in a single image. It is applicable in the detection of focused particles in optical tomography images and the further problem of selecting only the focused particles is addressed in Section 3.5.

The approach proposed in this paper, aims at the individual detection and measurement of particles in single images with minimal user-intervention. The role of appearance-based approaches is studied in the effort to provide a generic approach to particle detection that is invariant to different types of particles and that is robust to local changes of particle appearance, due to reflections, occlusions, shadows, and highlights. Of special interest to this work is the measurement of dense particle dispersions as conventional methods suffer from weaknesses in this condition. If detection is successfully performed, the motion and disformation of particles can then be accurately monitored, due to the fine resolution of optical sensors (e.g. [20–23]). Given a high enough frame rate to assume motion continuity, contour disformation can be accurately tracked using deformable contours [24] and particle trajectories can be estimated through the Kalman family of stochastically optimal estimators [25].

This paper deals with particle detection and size determination in dense dispersions using an appearance-based approach. As a first step, only roughly spherical particles are considered, a choice which reduces computational effort and allows to get insight in other critical aspects of the proposed approach. A relevant application of high technological interest is monitoring of the decay of wet foams, e.g. in food systems, with time. Extending the analysis to other shapes is straightforward and can be easily implemented. Work on this topic as well as the analysis of particle motion and tracking is underway and will be the subject of subsequent publications.

The remainder of this paper is organized as follows. In Section 2, the current state-of-the-art on image analysis techniques is presented and the specific needs for the present application (dense dispersions) are depicted. In Section 3, the technical features of the proposed appearance-based approach are explained and ways to optimize its performance are proposed. In Section 4, the method is enhanced to operate with multiple prototypes and also automatically synthesize novel ones, which are more characteristic and increase detection rates. In Section 5, the analysis is implemented to foam images taken at different time intervals and the results are discussed with respect to both the significance of the obtained information and also the physical mechanism(s) dictating foam decay. Finally, in Section 6 conclusions are discussed and future directions of this work outlined.

2. Previous work

Particle detection and measurement has been traditionally performed in a, more or less, manual manner in different domains of study (e.g. [21,22,26–28]). The problems in foam

imaging analysis are comprehensibly described in [19,29] a review of methods for the detection and measurement of particles can be found. As it can be therein verified, similar image analysis techniques can be utilized to measure particles in different states.

Several of the existing approaches to particle measurement are not suitable for the detection of densely dispersed particles, because they assume that the targets are imaged clearly and do not overlap each other in the image. Images of overlapping particles produce errors in approaches that either track the contour of a particle, or group its pixels, because a single – and bigger – particle is detected instead of two or more (e.g. [30]). In [27], the edges corresponding to a detected circle have been polynomially interpolated. The extraction of an energy-minimizing closed-contour, or “snake” [31,32], has been applied [33,34] but only in single particle measurement or sparse dispersions. In dense dispersions, initializing the contour is a further issue since the particle has to be detected in the first place. Another algorithmic approach attempts to cluster pixels in groups that correspond to the same particle, based on spectral properties (e.g. color or intensity) and proximity [20,22,33]. Beside the erroneous behavior in cases of overlap, pixel-grouping methods require highly controlled image acquisition so that pixels corresponding to the same object exhibit the same photometric values—a requirement not always simple to meet.

In a different type of approach, the idealized contour of a particle is utilized as an exemplar. A generic and straightforward model-based approach to the detection of image contours of known shape is the Hough transform [35], which operates in the image obtained from detecting edges in the original (see Section 2.1). In this context, Canny [36] and Laplacian edge detection have been utilized ([37,20], respectively). When the method is formulated for circles, it collects votes from edges that occur on the circumference of hypothesized circles. The exhaustive evaluation of all hypotheses is avoided by considering only plausible ones, based on the detected edges. The hypotheses that collect enough votes are considered then as detected circles. Hough transforms are utilized to detect circular and square particles in [38], but again for a few isolated targets only in the acquired image. This approach faces significant performance degradation in dense dispersions of particles, because the edges of densely arranged and/or overlapping particles vote for spurious circle hypotheses. To this difficulty adds the fact that often the image’s edges do not unambiguously match the assumed geometrical model for the target (e.g. a circle in this case). The difficulty is due to image noise and illumination artifacts (e.g. clutter, shadows/highlights, occlusions), because such phenomena alter the shape of the particles and also create spurious circular shapes in the image that do not correspond to particles. The results obtained by the Hough transform (see Fig. 1) indicate that using a model of the target significantly increases the robustness of detection, however a circle proves too simple to cope with the complexity of the visual appearance of encountered in generic images. Nevertheless, a detection-conservative version of this approach is found helpful in initializing the method proposed in this paper and described in more detail at the end of this section.

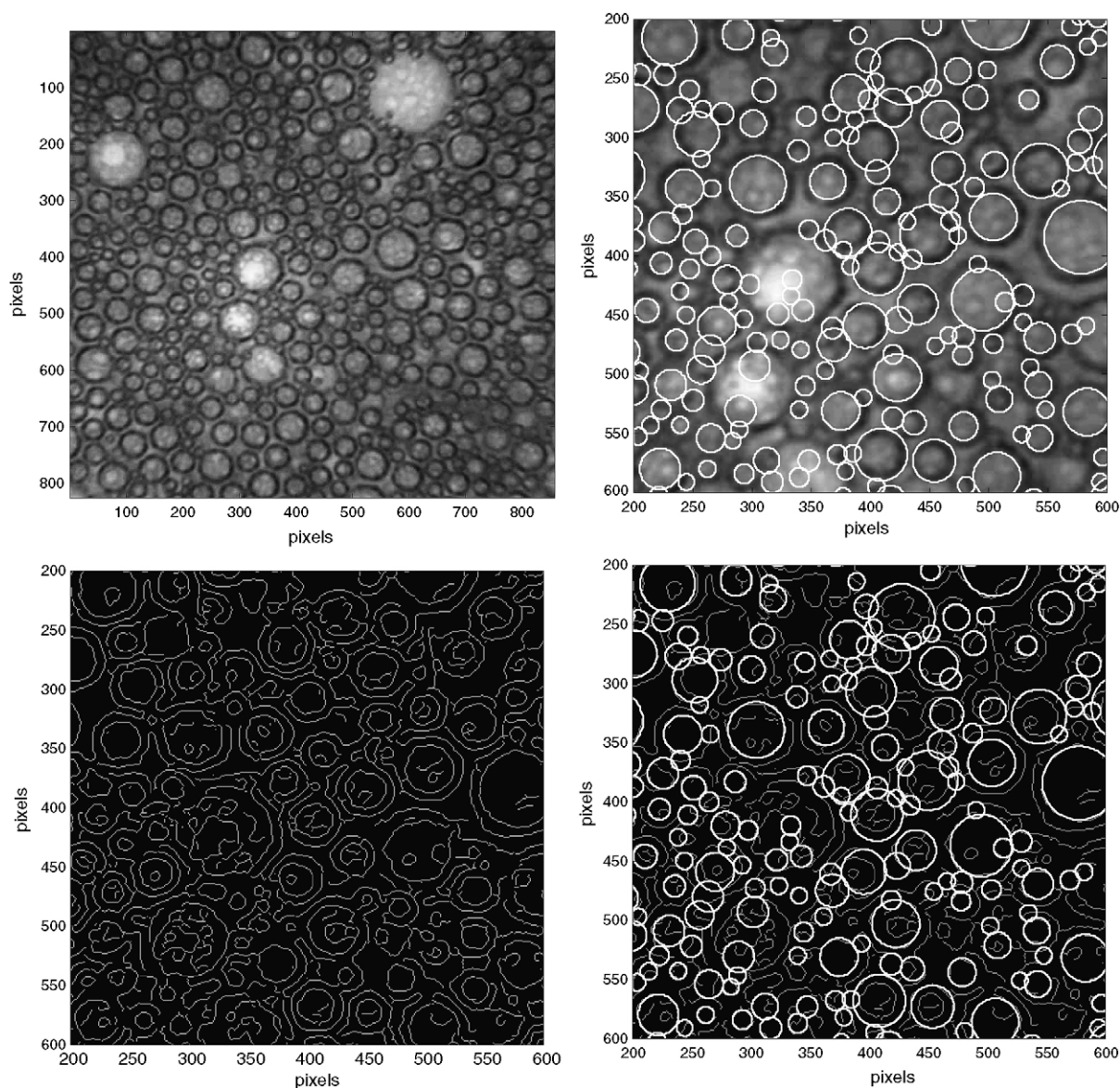


Fig. 1. Detection of particles (bubbles) utilizing the Hough method in an image (top left) of a dense dispersion (wet foam) and detail of the image center and corresponding edges, with the detected circles superimposed (rest of images). The votes for each hypothesized circle are equal to the number of edge-pixels that occur along its circumference. In the edge image, particles are not always depicted as perfect circles and thus spurious circles (e.g. at 450, 250) can collect a highest score than correct ones.

An appearance-based way to determine if a particle appears within an image region is the similarity comparison of this region with a *prototype image* of the particle. This technique is usually referred as *template matching*. To perform the comparison, metrics of image region similarity are employed that compare intensity values of the image region with the prototype. Two such metrics are the sum of absolute differences and the sum of squared differences. Another metric utilized in comparing the similarity of two image regions of the same size is to compute the normalized cross-correlation, *ncc*, of their sample populations (of color or intensity). The *ncc* metric is invariant to local variations of illumination and, as a result, it provides the same value despite the possible occurrence of the candidate target as relatively darker or brighter than the prototype. Its

formula is

$$\text{ncc} = \frac{\sum_{x,y} [f_1(x,y) - \bar{f}_1][f_2(x,y) - \bar{f}_2]}{\sqrt{\sum_{x,y} [f_1(x,y) - \bar{f}_1]^2 \sum_{x,y} [f_2(x,y) - \bar{f}_2]^2}}, \quad (1)$$

where f_1 is the prototype image, f_2 the compared image regions, and $\bar{f}_{1,2}$ are the respective mean values of these regions. The denominator normalizes the value set of the function to be in the region $[-1, 1]$, with negative values indicating anti-correlation. A review of this type of several correlation-based methods can be found at [39]. To date, however, such approaches have been only tried [40–43] in the context of sparse particle dispersions

and for simple particles of similar or the same size. Handling particles of various sizes and complex form requires further scale analysis and handling of multiple prototypes, as shown in this paper.

2.1. Application of the Hough transform to the detection of densely dispersed circular particles

A sophisticated implementation of the Hough approach to circular particle detection can be the following:

- (1) Perform Canny edge detection.
- (2) Perform circular Hough transform on the edge image.
- (3) Perform least-squares optimization with circle pixels (from Hough) to find best-fitting circles.

Step 1 is enhanced by employing a *scale-space* analysis [44] in the computation of the image gradient. In particular, the gradient is computed at the scale that best matches the size of the local structure [45]. Utilizing such an approach image edges are detected in the image with increased clarity and robustness.

Fig. 1 shows that spurious maxima occur in Hough space, due to the voting of circle hypotheses by edges that occur on some hypothetical circle but not on the outline of a particle—a spatial arrangement that becomes more probable as density increases. Discriminability of valid maxima in Hough space is further reduced by the presence of shadows, highlights, and occlusions, which may occur in such an arrangement that give rise to circular image structures that do not correspond to real particles. As a result, either too few or too many particles are detected depending on how high the threshold is set on the number of votes required to detect a circle. Some further discrimination can be obtained by invoking low-level heuristics such as *completeness* [46], or higher-order continuity information. On the other hand, a few circles can be reliably detected if the highest scoring maxima in Hough space are selected. The corresponding image edges are then erased and the detection is repeated. Iterating this process for a small number of repeats can be utilized to reliably detect a portion of the targets. This version, although very conservative in detecting particles, is utilized in our experiments for the initial detection of $\approx 20\%$ of the total detection targets, which are then used as exemplars for the detection of the rest.

3. An appearance based approach

In the proposed approach, particles are detected based on their appearance, rather than on a model (e.g. circle). A particle is selected from the original image, I , and utilized as a prototype to detect the rest. To do so, its image region is compared with every possible pixel-neighborhood in the original image—mapping similarity values to image coordinates. In this similarity function, a similar image neighborhood of the same size appears as local maximum (LM), whose locus indicates the coordinates of the matching image region. Detecting similar particles, but at a different size or posture, can be achieved by respectively resizing or rotating the prototype. Each of the invariances to size and rotation, increases computational complexity and, therefore, in the last subsection techniques that target its reduction are proposed.

3.1. Single prototype, single scale

In the simplest formulation, the targeted particles are of equal size, let $w \times w$, to the prototype P : for each pixel \vec{p} in I , a $w \times w$ neighborhood, N , around \vec{p} is considered. The $ncc(N, P)$ value is then associated with location \vec{p} . The result is a “similarity map” S of equal size to I (see Fig. 2). In this image, matching neighborhoods appear as spatially local similarity-maxima. The similarity value map to be smooth, because neighboring pixels correspond to overlapping regions with similar pixels in common positions. A pixel of S is a LM if its value is greater than that of the eight neighboring pixels. A thresholding of S precedes the LM detection in order to exclude LMs of very low ncc value.

In dense dispersions of bubbles, an important detail of implementing the ncc function is to estimate similarity for circular ($\rho = w/2$) image patches, because rectangular ones tend to partially image neighboring particles.

3.2. Multiple scales

To detect visually similar areas to P but at a different scale, P is interpolated at the new size, i.e. $w' \times w'$. The procedure is repeated for a range R of sizes and the generated similarity maps are stacked to create V , a similarity scale-space (see Fig. 3). LM

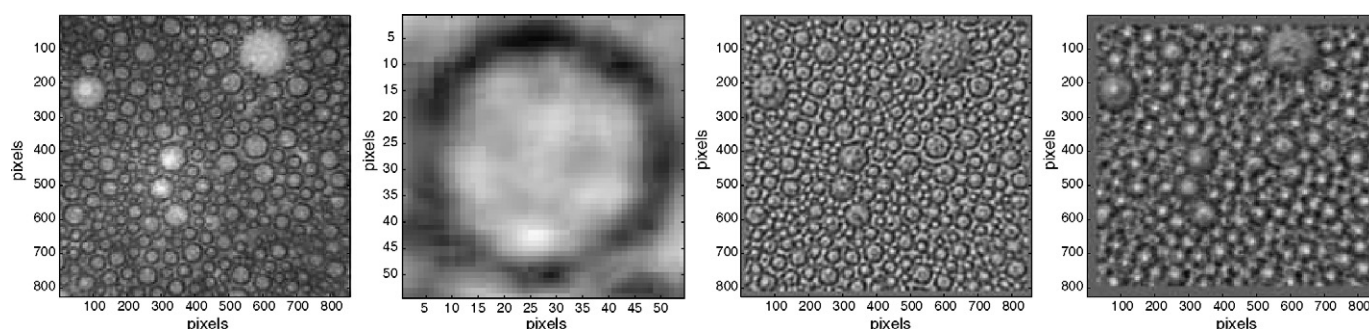


Fig. 2. Original image and prototype (left two) and similarity maps (right two) for a 25×25 and 50×50 pixel (rightmost) resampling of the prototype. Similarity is not evaluated in a $\lceil w/2 \rceil$ -pixel border around the image, because the $w \times w$ neighborhoods centered at these loci exceed the limits of I .

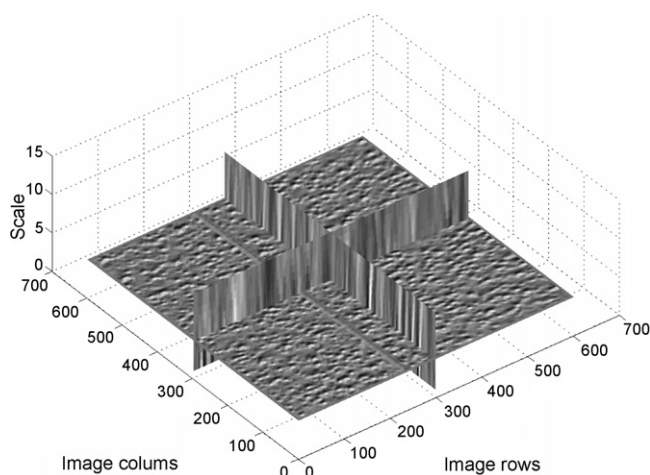


Fig. 3. The similarity scale-space generated by stacking similarity maps obtained for increasingly dense resamplings of the prototype. A local maximum in this space corresponds to the size and the location of a matching neighborhood in the image.

detection is now performed in 3D neighborhoods of 26 *voxels*.¹ The 3D locus of the LM corresponds to image coordinates and particle size.

In practice, the computation above is implemented in a way that conserves memory, because generating and storing V may not be feasible when I and R are large. Thus, instead, V is “swept” along the scale dimension storing at any time only three similarity maps as follows: let r, c the pixel dimensions of I . A $r \times c$ index J is first zero-initialized to store the highest similarity value at each image locus and the size of the corresponding prototype. At a given scale k , the $r \times c \times 3$ matrix B contains the three $r \times c$ similarity maps S_{k-1}, S_k, S_{k+1} corresponding to scales $k-1, k, k+1$, in that order. Local maxima are computed only for S_k . For each LM whose similarity score is greater than that recorded at the same position in J , J 's is updated with its score and size (at that position). For the next scale, maps are shifted in B , S_{k+2} is placed in the last slot and the process repeated. The procedure is iterated for all scales in R , with k commencing from the second and terminating at the penultimate. At the end, non-zero values of J indicate the loci of the detected particles and their sizes.

3.3. Detecting rotated versions of the prototype

Evaluation of rotated versions of P can be utilized to obtain invariance of the similarity match to rotation. At each scale-space location (x, y, w) , the result stored in S is: $\max_{\alpha} [\text{ncc}(P_{\alpha}, I_n)]$, where P_{α} is P rotated by $\alpha \in [0, 2\pi)$ about its center and I_n the $w \times w$ image neighborhood at \vec{p} .

To obtain a rotated version of the prototype and still retain the, practically required, same kernel shape the prototype is resampled from I . The loci of the resampling are derived from the

initial, integer, sampling coordinates $\vec{p}_i = [p_i x, p_i y]^T \in I_n$ but transformed as $R(\alpha) * (\vec{p}_i - \vec{p}) + \vec{p}$, where $R(\alpha)$ is the rotation matrix for angle α . Intensity samples are obtained at these loci by interpolating I . In our experiments rotation was not utilized, relying on the omnidirectional symmetry of the targets, to reduce computational complexity.

3.4. Performance optimization

The computational cost of computing the similarity map of P to I is $O_1 = O(m n w^2)$, where $m \times n$ I 's dimensions. This complexity scales to $O(n_{\alpha}) \cdot O(n_s) \cdot O_1$ for n_{α} rotations and n_s scales.

A first approach in performing the computation efficiently is based on [43], but extends the optimization even further by utilizing convolution (as a multiplication in the spectral domain) to precompute the intermediate results of image mean and variance that are required in Eq. (1). To retain the shape of the compared neighborhoods the convolution kernel is circular, instead of square. The continuity of the similarity function across scale-space facilitates a coarse-to-fine approach to the detection of LMs that reduces the performed ncc comparisons. Scale-space volume V is sampled coarsely by assuming a sparser discretization of scale (w) and space (pixels) and LMs are then detected at this, coarsest, scale-space discretization. Iteratively, this discretization is refined by a factor of 2, but only at the neighborhoods of the previously detected LMs. Speedup in this case is content dependent and determined by the amount of LMs. In our experiments, LMs were still robustly detected after 2 coarsenings of the discretization and the obtained speedup was in the range of 4–6. Fig. 4 illustrates the approach. The first scale is computed exhaustively, but subsequent ones are computed only at the regions where the previous scale exhibited a high similarity value (the bright regions in the images).

An additional complexity optimization, refers to images of high resolution. Prior and independently to the above optimization, the image is subsampled at a sparser resolution. The basic characteristics of the targets still survive this transformation. After LMs are detected in the lower resolution image, a final correlation step is performed to map the localization results back to the high resolution image. For a resolution reduction by a factor of β , a $(1 + \lceil \beta/2 \rceil)^3$ neighborhood of the scale-space of the original image is considered. Speedup is then $O_1 + \beta^3 O(\beta^3)/O(\beta^3)$. In our experiments, $\beta = 1/3$.

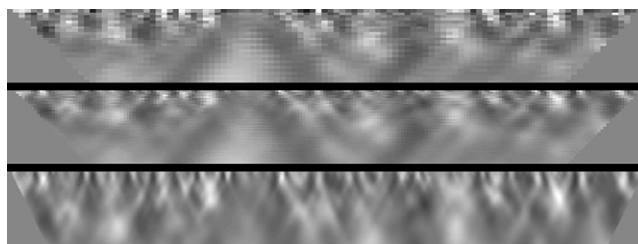


Fig. 4. Coarse-to-fine detection of particles. The three images show a section of the similarity scale-space generated by an image and a prototype. The horizontal axis corresponds to an image row and the vertical to scale.

¹ In this case, voxel (or “volumetric-pixel”) is the 3D equivalent of the (2D) pixel and is referred to as a volume element that represents a value on the regular grid of the three-dimensional similarity scale-space.

Another performance improvement refers to increasing the precision of detection, rather than reducing the computation to obtain this detection. The localization of targets with subpixel accuracy was obtained by fitting a circle $(x - a)^2 + (y - b)^2 = \rho^2$, in the least-squares sense to the set of edges $\{(x_i, y_i)\}_{i=1}^m$, $m \geq 3$ that occur nearby the circumference of the detected target. The result is obtained from the result of the search for the $[x, y, \rho]$ tuple that minimizes the $E(x, y, \rho) = \sum_{i=1}^m (L_i - \rho)^2$ energy function, where $L_i = \sqrt{(x_i - a)^2 + (y_i - b)^2}$ (see [47] for an implementation).

Finally, two practical acceleration techniques are proposed. The first refers to the utilization of multiple prototypes (see Section 4). Once targets have been estimated for the first prototype, the search for the succeeding ones is restricted to image regions for which a target has not been yet detected. The second technique refers to temporally continuous image sequences, where the result of the previous frame is utilized to restrict the search in the next frame. The detected targets will represent the majority of targets in the image and its remainder is then processed as in the above technique.

3.5. Focus

The particular wet foam images that are analyzed in this paper, represent foam bubbles that are in contact with the transparent wall of the container and so lie at a known – and more or less constant – distance from the camera. That is, the majority of the recorded particles were within the employed depth of field. Thus the image size of particles could eventually be measured in actual units, by accounting for the above distance and the intrinsic camera parameters (focal length, pixel size and image resolution). Further accuracy can be obtained by accounting for the perspective and lens distortion, as well. Yet, a few bubbles were still out of focus and therefore have to be excluded from the analysis. This was so because between neighboring wall bubbles, silhouettes of bubbles further inside the foam were discerned. In addition, in more generic experiments the distance of particles from the camera may not be a priori known. To deal with situations where particles lie at appreciably different focal lengths the software provides the means to select only in-focus particles. Simple standard techniques have been incorporated for this. A cue to the distance of an imaged particle is available from the sharpness, or focus accuracy, by which particles appear in images. If the camera system is focused at distance R , then only particles occurring at that distance (R) from the optical center will be focused on the image plane. Thus, the measurement process may – at least – select the focused particles and estimate their actual sizes.

The sharpness of the silhouette of a particle in the image, or otherwise the steepness of the variation that intensity undergoes at the corresponding image locations, is considered as a metric of the above cue and measured by the magnitude of the image gradient ($|\nabla I|$) at these locations. A per-particle metric of this sharpness can be formulated by integrating $|\nabla I|$ along the circumference of the particle in the image and normalizing for the length of this circumference, to equally treat particles of different sizes. In discrete images, the following formula can be

utilized:

$$\text{sharpness} = \frac{\sum_i^{N_c} |\nabla I(x_i, y_i)|}{N_c}, \quad (2)$$

where N_c is the number of pixels along the circumference of the particles image (a circle in the experiments presented in this paper) and x_i, y_i are the pixel coordinates of the image locations of the corresponding N_c pixels. A threshold τ_f can be then utilized to select the focused particles.

The threshold-setting process can be tedious since the optimal threshold value may heavily depend on the image type. Therefore, a technique is employed to increase the automation of the above process. The detected particles are visually sorted in decreasing order of sharpness. Then, the user selects the least focused particle that may be included in the set of particles to measure and τ_f is automatically set at the sharpness value that was obtained for the selected particle. In consecutive measurements, the system remembers the previous setting of the threshold and offers the corresponding value as a default value which, however, the user may update.

4. Detecting multiple patterns

Often the targets to be detected in I exhibit differences regarding their visual appearance, due to the imaging apparatus or due to actual differences of their structure. A way to overcome this difficulty is to utilize multiple prototypes, obtain individual results and, then, merge them. In this section, the above process is studied and a way to automate the selection of multiple prototypes is proposed.

4.1. Merging results from multiple prototypes

Utilizing multiple prototypes is performed by repeating the procedure of Section 3 for each P_i and concatenating the obtained results. In this process, however, a particle may not only be detected more than once but also in slightly different arrangements of $[x, y, \rho]$. A method to merge the individual results is proposed that selects the most accurate out of multiple localizations of a target.

The first step is to group the N detected particles based on the target that they indicate. Multiple detections of a single target are detected as being overlapping to a great extent (e.g. $> 30\%$, in our experiments). A $N \times N$ Cartesian matrix, E_{ij} , is then generated, which represents the percentage of overlap area between any two particles i and j . For two circular targets (\vec{o}_i, ρ_i) and (\vec{o}_j, ρ_j) overlap is signified by comparison of their center distance $\delta = |\vec{o}_i - \vec{o}_j|$ to their radii difference $|\rho_i - \rho_j|$. If overlapping, the above percentage is given by the ratio of the common area of the two targets over the area of the greatest circle. This common area is the intersection of two circles which can be computed as the sum of the two half-lens areas in each circle: $h(\rho_i, \tau) + h(\rho_j, \tau)$, where $\tau = (d^2 - \rho_j^2 + \rho_i^2)/2\delta$ and $h(\rho, \tau) = \rho^2 \cos^{-1}(\tau/\rho) - \tau(\rho^2 - \tau^2)^{1/2}$. The detected targets are grouped in sets that correspond to the same particle, by

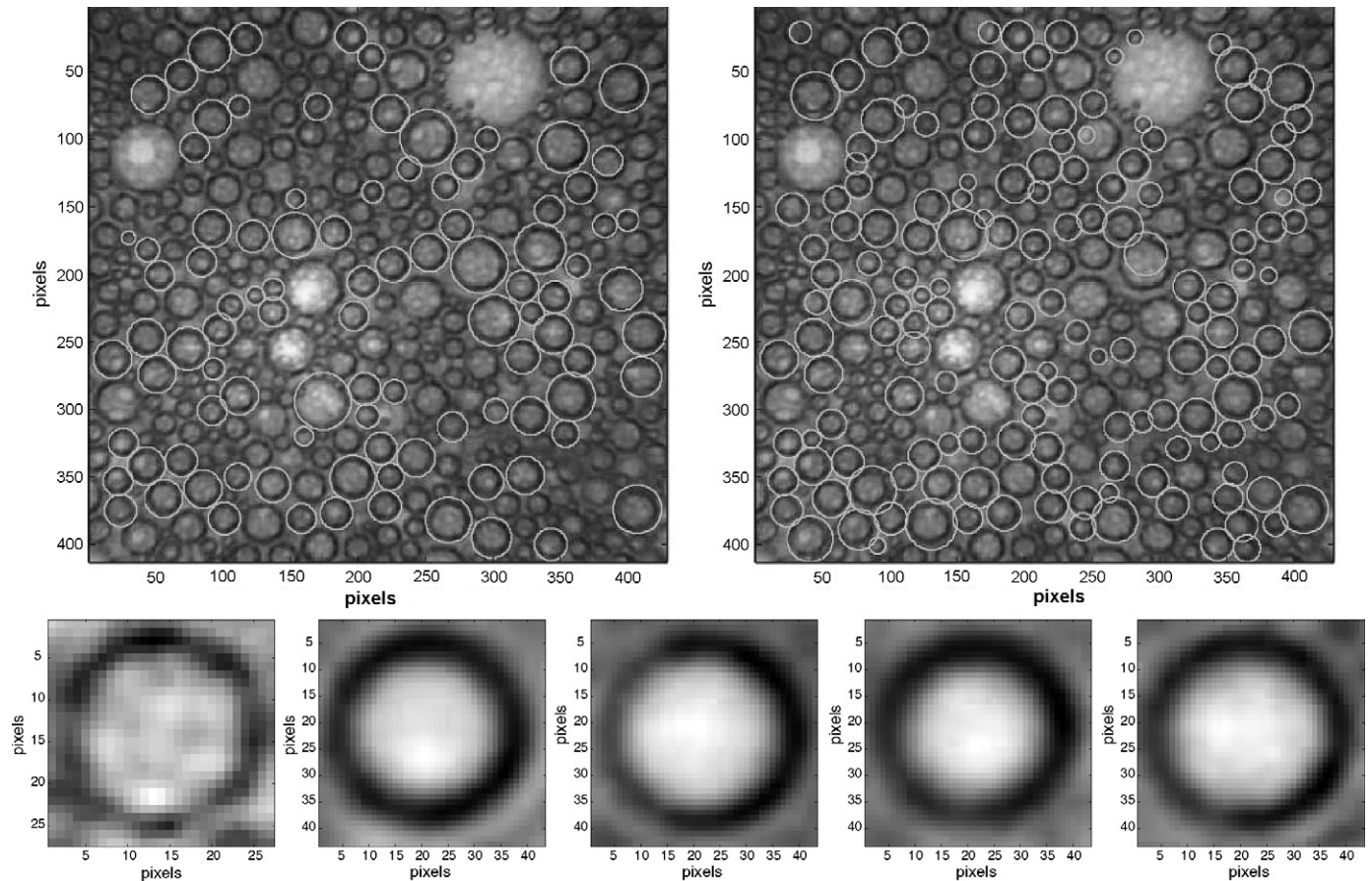


Fig. 5. Utilization of synthetic prototypes. Top left image shows the detection of particles with the bottom left prototype. The rest of the prototypes in the bottom row are synthesized from this result. When the synthetic prototypes are utilized, more particles are detected (top right).

recursively searching E for all the circles that overlap each other at the same image region.

The next step is to select a representative for each group, that best fits the detected target. The selection is based on the completeness metric which is the ratio of the number edge elements along the circumference of the circle over the arc length of this circumference. In this case, completeness is a better criterion than utilizing the ncc, because it is based on edges that indeed belong to the particle.

The particles are outputted in tuples of $[x, y, \rho]$ that represent the detected circles. This representation permits topological measurements such as for example the image area “occupied” by particles or not. In our wet foam, it may be of interest to compute the fraction of pixels imaging liquid (lamellae and plateau borders) over the rest imaging gas (bubbles), for each horizontal image line. An efficient way to perform this computation is to scan all image rows and at each row Y calculate the pixel occupied by the detected circles. For each circle $O(x, y, \rho)$ that $|y - Y| < \rho$ this area is $\sqrt{\rho^2 - (y - Y)^2}$, else this area is 0.

4.2. Automating the prototype selection process

Manually selecting prototypes for target detection can be a tedious process, especially if the visual diversity of targets is large. To reduce human intervention, the circular Hough transform can be utilized, as described in Section 2.1 in order

to reliably obtain some initial prototypes. The images of these targets are then analyzed to generate new, synthetic prototypes as follows.

All of the extracted image patches are initially interpolated to the size of the largest target, let $w_M \times w_M$. The interpolated images are then considered as vectors in w_M^2 space, whose w_M^2 components are the intensity values within the extracted patch. Clustering of these data is then performed, assuming that visually similar vectors will be classified in the same cluster. The utilized clustering approach is *K-means* [48] in combination with the Schwarz criterion [49] to automatically determine the number of clusters. For each derived cluster, the vector that minimizes the distances in M^2 -space is computed as the eigenvalues from a principal component analysis (PCA). Each such vector is considered as characteristic of the cluster and utilized as a new prototype. This prototype may not be found in the image since it is synthesized from the w_M^2 that comprise this mean vector. The procedure is illustrated in Fig. 5.

5. Implementation and measurements

5.1. A prototype system implementation

The similarity matching techniques presented in this paper were compiled in a standalone computer application with a graphical user interface, created in *Borland's Builder C++ 6*.

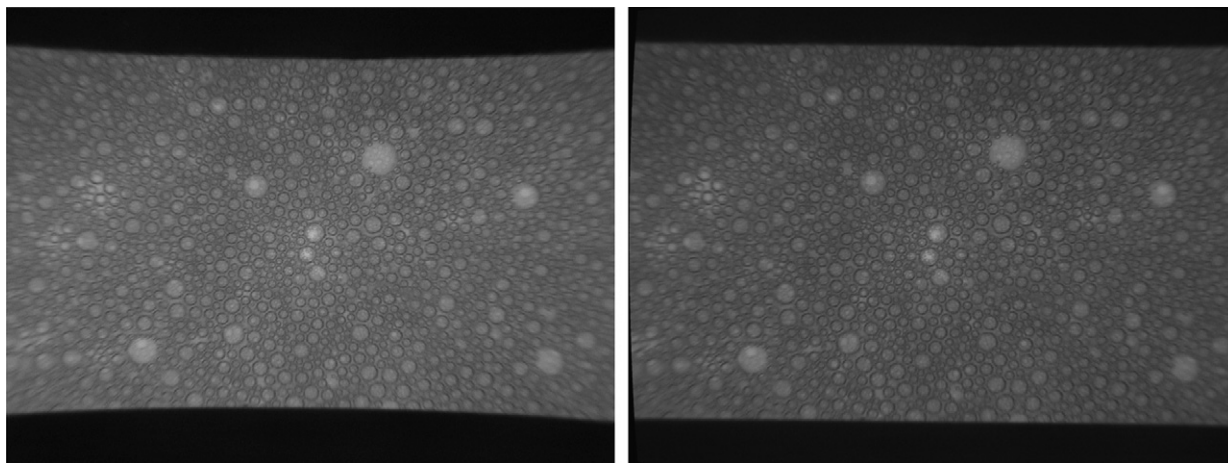


Fig. 6. Result (right) of the automatic compensation for radial distortion on an original image (left), based on the assumption that the distorted horizontal lines in the image are straight in reality.

Prior to the main analysis images were preprocessed to standard error-reduction and edge-enhancement, but were also warped to compensate for the radial distortion of the optical lens. This compensation tends to increase both the accuracy of measurement and the particle detection rate. To perform this correction an estimation of the intrinsic camera parameters was required. This estimation can be obtained either manually or automatically through a calibration process. Automatic calibration requires that some particular feature is present and detected in the image and the accuracy of calibration is determined by the accuracy by which this feature was localized. A simple and effective approach is to utilize straight lines that are detected in the image for this feature as in [50] (demonstrated in Fig. 6). In cases where such features are unavailable, or for greater accuracy, manual estimation is preferred. The process is typically tedious, but can be simplified by software utilities (e.g. [51]).

Using the graphical interface, the user selects a few prototype particles (e.g. 10) to bootstrap the detection process. In addition, some initial prototypes are reliably extracted as in Section 2.1. This initialization process requires less time as more images are processed, because the system creates a library of prototypes to be utilized in the forthcoming measurements. To increase efficiency, this library is proposed to be comprised from the prototypes synthesized after the first detection stages (see Section 4.2). After the initial set of prototypes is determined, the correlation procedure of Section 3 is performed. The detected particles are then indicated in the original image. If detection of the particles is not complete the user is prompted to indicate some more prototypes, out of the particles that were not detected and the procedure is repeated. Finally, the user may correct the result by individually deleting or adding particles.

In Fig. 7 the user interface to the above procedure is shown. In the top row, the user selects three prototypes (left) to detect several but not all particles (right). In the bottom row, adding two more prototypes (left) increases the number of detected particles (right). At the top left part of the above screen prints, detected particles are indicated in the original image. The bottom right part of these screen prints shows the prototypes. In the user inter-

face, the detected particles are classified by size in three panels, corresponding to small, medium, and large. Within each panel, the detected particles are sorted by similarity to the prototype. The user has the option of automatically rejecting the group of particles that are more dissimilar to the prototype than an indicated particle in these panels, or individually.

The difficulties encountered using the prototype implementation give rise to future research topics that are further discussed in Section 6. The most crucial is the relatively large computational time of the correlation step, which on average required ≈ 15 min for the measurement of the $\approx 80\%$ of the bubbles in a 5×10^6 pixel image.

5.2. Measurements

Foams were generated by whipping air into 300 ml of a 0.5% (w/v) soya protein (VIOTREK AVEE) and 0.10% (w/v) xanthan gum (SIGMA) solution using a Sunbeam Mixmaster mixer for 10 min at 900 rpm. The pH of the solution was at its natural value, 6.9, without any adjustment. Xanthan gum was used to increase the viscosity of the solution. Right after whipping the foam was decanted in a cylindrical test vessel with inner diameter 7.0 cm and height 17 cm. The test vessel was made of Plexiglas to allow optical observations. High resolution photographs of the foam were taken at regular intervals at the mid height of the vessel using a still camera (Canon, EOS 350D, 8 Mp) equipped with proper magnification lenses (Pentax, FA100 macro, F2.8). A dual probe fiber optic system (HAISER Macrospot 1500) supplemented with thin fiber extensions was employed to illuminate the foam uniformly from the back. The field of view was $1.5 \text{ cm} \times 1.5 \text{ cm}$ which assured that several bubbles would be contained in the image even at long times after foam formation when bubbles become excessively large ($d \approx 1.5 \text{ mm}$). Bubble sizes were determined from the images to obtain the bubble size distribution. Only sharp focus/clear edge bubbles were selected from the population of each image for the analysis. The selected bubbles span evenly across images and always include above 80% of the entire population. This represents more than 1700 and 400 bubbles for short and long times, respectively.

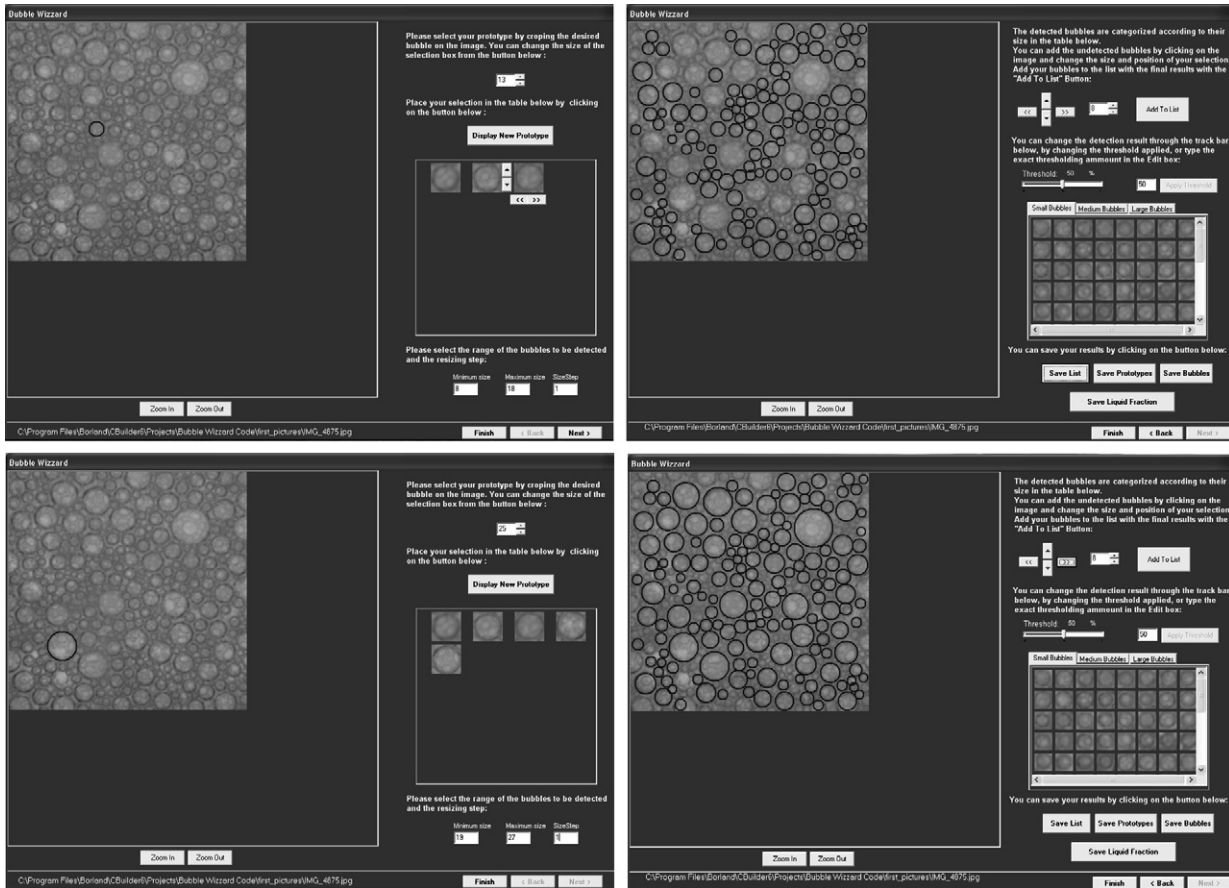


Fig. 7. The user interface that was created to access the proposed method’s functionality.

Fig. 8 shows the variation of bubble size distribution with respect to time as determined from the analysis of the photos. For clarity, bubble sizes are divided into four distinct classes (bins) spanning between 250 and 1250 μm . In fact, there are also a few bubbles below and above these limits but their number is so small that do not affect the distribution. Initially the foam is quite homogeneous with more than $\approx 90\%$ of the detected bubble population between 250 and 500 μm . The situation does not change much for the first 10 min. Sometime between 10 and 20 min, a small but clear alteration occurs with the smaller bubbles to partially vanish in favor of larger ones while remaining the dominant population ($> \approx 80\%$) in the foam. After that

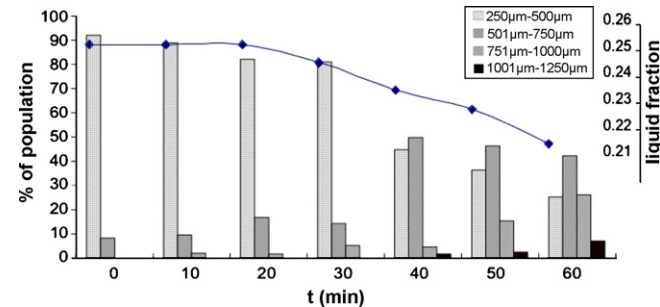


Fig. 8. Variation of bubble size distribution (bars) and average liquid fraction (line) of the foam with respect to time.

moment and up to 30 min, again no drastic activity is observed. Suddenly, at some instant between 30 and 40 min a large size redistribution takes place. This is manifested by the great reduction of the smaller bubbles (250–500 μm) and the sound increase of the second class of bubbles (500–750 μm). In addition, very large bubbles (1000–1250 μm) appear for the first time. From that moment on, there is a gradual reduction of the two smaller size-classes and a progressive increase of the two larger ones.

For foam bubbles containing air, bubble coarsening may be a mechanism competing effectively to liquid drainage. To what extent which of the two mechanisms control foam decay is not clear as it depends on several characteristics of the system. Yet, this is beyond the scope of this work. Fig. 8 displays also the time evolution of the average liquid fraction in the entire foam column calculated from global volumetric measurements of the instantaneous foam and drained liquid volumes. For such wet foams (typically met in food applications) having a considerable height, capillary hold-up effects at the bottom of the foam can be neglected and vertical liquid fraction gradients practically vanish (e.g. [52]). Thus the average liquid fraction of the foam column may be compared to local information from the photos. In Fig. 8, up to 20 min virtually no change in liquid fraction is observed being followed by a rather steady decline at longer times. Apparently, liquid fraction variations do not reflect the stepwise alterations taking place in the bubble population of the foam and more work is needed to understand the underlying

phenomena. For this, advanced image analysis tools such as the present are necessary.

6. Conclusion

In this paper, the template matching approach for the detection of particles was extended to operate in multiple scales and with multiple prototypes. In addition, techniques for increasing its computational efficiency and methods to reduce user-intervention were introduced. The techniques were implemented in a stand-alone piece of software which was then utilized to analyze the evolution of bubble size distribution in a typical food (wet) foam. Comparisons between the evolution of bubble size and liquid fraction in the foam demonstrate that accurate optical determination of bubble size distribution is important in order to interpret phenomena controlling foam decay.

Underway is research is to implement the most computationally demanding operations to be executed in commodity graphics hardware (or the Graphics Processing Unit), to further accelerate the present software. This approach has been recently gaining in popularity, due advances in parallel graphics hardware (see [53]).

References

- [1] R.M. Carter, Y. Yan, S.D. Cameron, On-line measurement of particle size distribution and mass flow rate of particles in a pneumatic suspension using combined imaging and electrostatic sensors, *Flow Meas. Instrum.* 16 (2005) 309–314.
- [2] R.A. Rahim, P.J. Fea, C.K. San, Optical tomography sensor configuration using two orthogonal and two rectilinear projection arrays, *Flow Meas. Instrum.* 16 (2005) 327–340.
- [3] S. Devasenathipathy, J.G. Santiago, K. Takehara, Particle tracking techniques for electrokinetic microchannel flows, *Anal. Chem.* 74 (15) (2002) 3704–3713.
- [4] F. Scarano, A super-resolution particle image velocimetry interrogation approach by means of velocity second derivatives correlation, *Meas. Sci. Technol.* 15 (2000) 475–486.
- [5] K.T. Kiger, C. Pan, PIV technique for the simultaneous measurement of dilute two-phase flows, *J. Fluid Eng.* 122 (4) (2000) 811–818.
- [6] W. Cheng, Y. Murai, F. Yamamoto, Estimation of the liquid velocity field in two-phase flows using inverse analysis and particle tracking velocimetry, *Flow Meas. Instrum.* 16 (2005) 303–308.
- [7] F. Pereira, M. Gharib, D. Dabiri, D. Modarress, Defocusing digital particle image velocimetry: a three-component three-dimensional DPIV measurement technique. Application to bubbly flows, *Exp. Fluid* 29 (7) (2000) 78–84.
- [8] H. Zara, V. Fischer, J. Jay, R. Fouquet, E. Tafazzoli, G. Jacquet, High-speed video acquisition system applied to flow study, *Meas. Sci. Technol.* 9 (9) (1998) 1522–1530.
- [9] A. Stitou, M.L. Riethmuller, Extension of PIV to super resolution using PTV, *Meas. Sci. Technol.* 12 (6) (2001) 1398–1403.
- [10] D. Bernard, G.L. Vignoles, J.M. Heintz, Modelling porous materials evolution, in: *X-ray Tomography in Material Science*, Kogan Page, 2000, pp. 177–192.
- [11] L. Salvo, P. Cloetens, E. Maire, J.J. Zabler, S. Blandin, J.Y. Buffiere, W. Ludwig, E. Boller, C. Bellet, D. amd Josserond, X-ray micro-tomography an attractive characterisation technique in materials science, *Nucl. Instrum. Meth. Phys. Res. B* 200 (2003) 273–286.
- [12] P.D. Thomas, R.C. Darton, P.B. Whalley, Liquid foam structure analysis by visible light tomography, *Chem. Eng. J. Biochem. Eng.* 56 (3) (1995) 187–192.
- [13] C. Monnereau, M. Vignes-Adler, Optical tomography of real three-dimensional foams, *J. Colloid Interf. Sci.* 202 (1) (1998) 45–53.
- [14] C. Monnereau, B. Prunet-Foch, M. Vignes-Adler, Topology of slightly polydisperse real foams, *Phys. Rev. E* 63 (6) (2001), 061402–10.
- [15] P.D. Thomas, R.C. Darton, P.B. Whalley, Liquid foam structure analysis by visible light tomography, *Ind. Eng. Chem. Res.* 37 (3) (1998) 710–717.
- [16] J. Lambert, I. Cantat, R. Delannay, A. Renault, F. Graner, J.A. Glazier, I. Veretennikov, P. Cloetens, Extraction of relevant physical parameters from 3D images of foams obtained by X-ray tomography, *Colloid Surf. A* 263 (2005) 295–302.
- [17] M.D. Montminy, A.R. Tannenbaum, C.W. Macosko, The 3D structure of real polymer foams, *J. Colloid Interf. Sci.* 280 (2004) 202–211.
- [18] J.M. Winter, X-ray computed tomography of ultralightweight metals, *Res. Nondestruct. Eval.* 11 (4) (1999) 199–211.
- [19] V. Bergeron, P. Walstra, Foams, in: *Soft Colloids*, vol. 5 of *Fundamentals of Interface and Colloid Science*, Elsevier, 2005, pp. 7–22.
- [20] R. Kulenovic, R. Mertz, P. Schäfer, M. Groll, High speed video flow visualization and digital image processing of pool boiling from enhanced tubular heat transfer surfaces, in: *Proceedings of the 9th International Symposium on Flow Visualization*, 2000, pp. 22–25.
- [21] I. Leifer, G. Leeuw, L.H. Cohen, Optical measurement of bubbles: system design and application, *J. Atmos. Ocean Technol.* 20 (9) (2003) 1317–1332.
- [22] A. Zaruba, E. Krepper, H. Prasser, B.R. Vanga, Experimental study on bubble motion in a rectangular bubble column using high-speed video observations, *Flow Meas. Instrum.* 16 (2005) 277–287.
- [23] K. Cheung, W. Ng, Y. Zhang, Three-dimensional tracking of particles and their local orientations, *Flow Meas. Instrum.* 16 (2005) 295–302.
- [24] J. Montagnat, H. Delignette, N. Ayache, A review of deformable surfaces: topology, geometry and deformation, *Image Vision Comput.* 19 (2001) 1023–1040.
- [25] P.S. Maybeck, Stochastic models, estimation, and control, in: *Mathematics in Science and Engineering*, vol. 1, Academic Press, New York, 1979, pp. 1–16.
- [26] N.J. Hepworth, J.R.M. Hammond, J. Varley, Novel application of computer vision to determine bubble size distributions in beer, *J. Food Eng.* 61 (2004) 119–124.
- [27] T.A. Kowalewski, J. Paklezb, A. Cybulskia, Particle image velocimetry for vapour bubble growth analysis, in: *Proceedings of the 8th International Conference Laser Anemometry Advanced and Applications*, 1999.
- [28] M. Bailey, C.O. Gomez, J.A. Finch, Development and application of an image analysis method for wide bubble size distributions, *Miner. Eng.* 18 (2005) 1214–1221.
- [29] Y. Zhu, B. Carragher, R.M. Glaeser, D. Fellmann, C. Bajaj, M. Bern, F. Mouche, F. de Haas, R.J. Hall, D.J. Kriegman, S. Ludtke, S. Mallick, P.A. Penczek, A.M. Roseman, F.J. Sigworth, N. Volkman, C.S. Potter, Automatic particle selection: results of a comparative study, *J. Struct. Biol.* 145 (1/2) (2004) 3–14.
- [30] A. Hasanen, P. Orivuori, J. Aittamaa, Measurements of local bubble size distributions from various flexible membrane diffusers, *Chem. Eng. Process.* 45 (2006) 291–302.
- [31] M.M. Kass, A. Witkin, D. Terzopoulos, Snakes: active contour models, *Int. J. Comput. Vision* 1988 (1988) 321–331.
- [32] T. Pavlidis, *Structural Pattern Recognition*, Springer, 1977.
- [33] S.B. Harvey, J.P. Bestz, W.K. Soh, Vapour bubble measurement using image analysis, *Meas. Sci. Technol.* 7 (4) (1996) 592–604.
- [34] D. Cheng, H. Burkhardt, Bubble tracking in image sequences, *Int. J. Therm. Sci.* 42 (7) (2003) 639–655.
- [35] J. Illingworth, J. Kittler, A survey of the hough transform, *Comput. Vision Graph. Image Process.* 44 (1) (1988) 87–116.
- [36] J.F. Canny, A computational approach to edge detection, *IEEE Trans. Pattern Anal. Mach. Intell.* 8 (6) (1986) 679–698.
- [37] T.A. Kowalewski, R. Trzciński, A. Cybulski, J. Pakleza, M.C. Duluc, Experimental analysis of vapour bubble growing on a heated surface, in: *Proceedings of the 3rd International Conference on Transport Phenomena in Multiphase Systems*, 2002.
- [38] Y. Zhu, B. Carragher, C.S. Potter, Automatic particle detection through efficient hough transforms, *IEEE Trans. Med. Imaging* 22 (9) (2003) 1053–1062.

- [39] W. Nicholson, R. Glaeser, Review: automatic particle detection in electron microscopy, *J. Struct. Biol.* 133 (2001) 90–101.
- [40] J. Frank, M. Radermacher, P. Penczek, J. Zhu, Y. Li, M. Ladjadj, A. Leith, Spider and web: processing and visualization of images in 3D electron microscopy and related fields, *J. Struct. Biol.* 116 (1996) 190–199.
- [41] Z. Huang, A. Penczek, Application of template matching technique to particle detection in electron micrographs, *J. Struct. Biol.* 145 (1/2) (2004) 29–40.
- [42] D. Cheng, H. Burkhardt, Template-based bubble identification and tracking in image sequences, *Int. J. Therm. Sci.* 45 (2006) 321–330.
- [43] A. Roseman, Particle finding in electron micrographs using a fast local correlation algorithm, *Ultramicroscopy* 3/4 (2003) 225–236.
- [44] T. Lindeberg, Scale-space theory: a basic tool for analysing structures at different scales, *J. Appl. Stat.* 21 (2) (1994) 224–270.
- [45] T. Lindeberg, Edge detection and ridge detection with automatic scale selection, *Int. J. Comput. Vision* 30 (2) (1998) 117–156.
- [46] B. Taboada, L. Vega-Alvarado, M.S. Cordova-Aguilar, E. Galindo, G. Corkidi, Semi-automatic image analysis methodology for the segmentation of bubbles and drops in complex dispersions occurring in bioreactors, *Exp. Fluid* 41 (2006) 383–392.
- [47] P. Schneider, D. Eberly, *Geometric Tools for Computer Graphics*, Morgan Kaufmann, 2004.
- [48] J.B. MacQueen, Some methods for classification and analysis of multivariate observations, in: *Proceedings of the 5th Berkeley Symposium on Mathematical Statistics and Probability*, 1967, pp. 281–297.
- [49] G. Schwarz, Estimating the dimension of a model, *Ann. Stat.* 6 (1978) 461–464.
- [50] F. Devernay, O. Faugeras, Straight lines have to be straight, *J. Mach. Vision Appl.* 13 (1) (2001) 14–24.
- [51] J.Y. Bouguet, Camera calibration toolbox for matlab, <http://www.vision.caltech.edu/bouguetj/calib.doc/>.
- [52] G. Maurdev, A. Saint-Jalmes, D. Langevin, Bubble motion measurements during foam drainage and coarsening, *J. Colloid Interf. Sci.* 300 (2) (2006) 735–743.
- [53] M. Pharr, R. Fernando, *GPU Gems 2*, Addison, Wesley, 2005.